Thickness effects in Mössbauer scattering experiments*

Bohdan Balko and Gilbert R. Hoy
Physics Department, Boston University, Boston, Massachusetts 02215
(Received 19 June 1974)

We have calculated the ^{57}Fe Mössbauer scattering line shape. These calculations include, in addition to the nuclear resonant scattering, consideration of electronic Rayleigh scattering, incoherent thickness effects, as well as angular distribution factors. These calculations are an extension and generalization of the results of Debrunner and Morrison, in order to describe a multilined Mössbauer pattern. Integration over all possible incident and outgoing γ- ray directions was carried out to obtain the line shape for powder scatterers. The theoretical predictions arising from these computations were checked under a variety of experimental conditions using natural and enriched iron metal and α-Fe_2O_3. In all cases it was found that consideration of incoherent thickness effects was necessary for understanding the results. Calculation and experiment showed that the line-intensity saturation effect in scattering is quite different from the ordinary transmission result. Our analysis also shows that the scattering spectrum is quite sensitive to the value of the recoilless fraction.

I. INTRODUCTION

Scattering experiments have been performed in the past to study a variety of physical phenomena. Considerable interest has been devoted to the study of interference effects between Rayleigh and nuclear resonant scattering[1-4] and experiments on the Debye-Waller factor.[5-7] Diffraction[8,9] and polarization[10] "effects" and the time dependence of the resonantly scattered radiation[11] have also been investigated. Scattering has been shown to be a more effective technique than transmission in the investigation of high-energy Mössbauer transitions.[12] The application of scattering geometry to the study of bulk samples[13] and surface effects[14,15] has also created some interest.

Theoretical investigations have dealt with interference effects,[16,17] lattice dynamics,[18] the application of scattering to the study of the magnetic structure of materials[19] and inhomogeneous electric fields,[20] and the effect of resonators acting collectively.[21,22]

Our primary concern recently has been the study of time-dependent hyperfine interactions using the selective-excitation double-Mössbauer technique.[23] However, it became clear that in order to use this technique we needed to understand Mössbauer scattering results. Because of the need to maximize the resonant counting rate, enriched scatterers are preferred. In order not to lose counts, the scatterers should also be physically thick. Thus, the necessary calculations must include these effects. In addition, it is important to be able to make such calculations when the ^{57}Fe nuclei in the scatterer interact with nonzero effective internal fields. The calculations presented here treat the case of an effective internal magnetic field. We make a detailed comparison between our theoretical scattering results and experimental spectra for these cases of so-called "split" thick scatterers.

II. THEORY

In this section we develop a method for calculating ^{57}Fe Mössbauer spectra using the scattering geometry shown in Fig. 1. When the 14.4-keV photons from the source impinge upon the scatterer, several types of scattering interactions are possible. The photon can be absorbed by a nucleus without recoil and then emitted with or without recoil. In addition, there are two other possible elastic scattering processes, namely, Rayleigh and Thomson scattering. These three processes can therefore lead to interference effects.[3] Also, there are the usual electronic absorption processes which can attenuate the beam as it passes through the scatterer. We can characterize the scatterer by its total linear absorption coefficient,

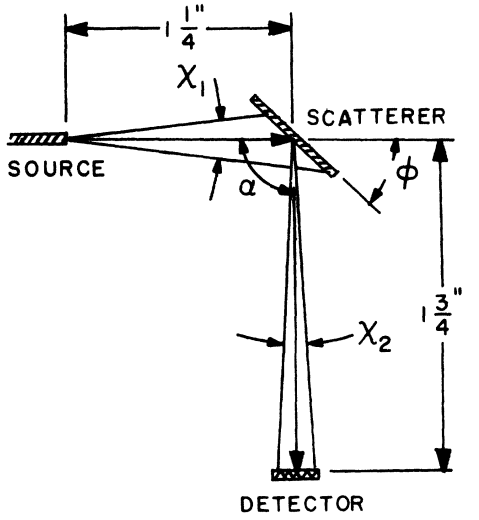

FIG. 1. Scattering geometry used in our experiments.

$$\mu_T(E) = \mu_M(E) + \mu_R + \mu_e \,, \tag{1}$$

where $\mu_M(E)$ is the nuclear resonant absorption coefficient, μ_R is the coherent nonresonant absorption coefficient including Rayleigh and Thomson processes, and μ_e is the electronic absorption coefficient which includes all the incoherent scattering processes.

Consider the situation as shown in Fig. 2. The intensity distribution of the source radiation, assumed to be Lorentzian, is $I(E,S)$,

$$I(E,S) = \frac{I_0(\frac{1}{2}\Gamma_b)^2}{[(E-E_0-S)^2+(\frac{1}{2}\Gamma_b)]} \,,$$

where S is the Doppler energy determined by the source velocity and Γ_b is the effective linewidth of the incident beam. The intensity of the radiation reaching a distance x into the scatter is

$$I_x(E,S) = I(E,S)e^{-\mu_T(E)\csc\alpha_1 x} \,. \tag{2}$$

Resonant nuclear absorption can take place at energies corresponding to the allowed nuclear transitions E_{ij},

$$\mu_M(E) = \sum_{i,j} \frac{nf\sigma_0(\frac{1}{2}\Gamma)^2}{(E-E_{ij})^2+(\frac{1}{2}\Gamma)^2} W_{ij}(\theta_1,\phi_1) \,, \tag{3}$$

where f is the scatterer's recoilless fraction, n is the number of resonant nuclei per unit volume, Γ is the natural linewidth, and σ_0 is the maximum resonant absorption cross section. The scattering angles are defined in Fig. 3(a). If the nuclear energy levels are pure m states, the angular distribution functions $W_{ij}(\theta_1,\phi_1)$ are[24]

$$W_{ij} = |C(I_e m_j | LMI_g m_i)|^2 |\vec{X}_L^M(\theta_1,\phi_1)|^2 \,. \tag{4}$$

Here the C's are the usual Clebsch-Gordan coefficients and the $\vec{X}_L^M$'s are vector spherical harmonics.

In general the energy distribution of the scattered radiation contains an interference term from the nuclear resonant and Rayleigh scattering processes. However, at a scattering angle $\alpha = 90°$ this interference term is zero.[3] We restrict our calculations and experiments to this case. We also disregard possible modifications of the line shape due to interference between individual neighboring lines[1,25,26] and coherent effects between neighboring nuclei.[21,22] Such contributions are in general small and only appear under very special conditions. For our case the contributing terms can be calculated separately and simply added.

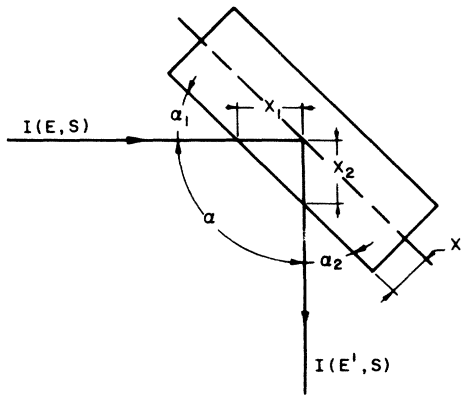

FIG. 2. Incident beam $I(E,S)$ interacts with the scatterer producing a scattered beam $I(E',S)$.

We first consider the nuclear resonant contribution. In general this term contributes a part from recoilless absorption and recoilless emission and another part from recoilless absorption and nonrecoilless emission. The energy distribution per unit length per unit solid angle of the radiation scattered recoillessly at x by the resonant process is

$$\frac{dI_M}{dx}(E',S) = \int dE\, I_x(E,S) nf \frac{d^2\sigma_M}{dE dE'} \,. \tag{5}$$

Following Boyle and Hall[27] we can write the differential scattering cross section as

$$\frac{d^2\sigma_M}{dE dE'} = \sum_{i,j,i'} \frac{f\sigma_0 W_{ij}(\theta_1\phi_1) W_{ji'}(\theta_2\phi_2)(\frac{1}{2}\Gamma)^2}{(1+\alpha')[(E-E'+\Delta_{ii'})^2+(\frac{1}{2}\gamma)^2][(E'-E_{ij}-\Delta_{ii'})^2+(\frac{1}{2}\Gamma)^2]} \,, \tag{6}$$

where α' is the internal-conversion coefficient, γ is the linewidth due to the source intensity and hence is very small, and we have allowed for absorption between the nuclear levels $E_i^g \rightarrow E_j^e$ to result in the decays $E_j^e \rightarrow E_i^g$ and $E_j^e \rightarrow E_{i'}^g$. $E_{ij} = E_j^e - E_i^g$ and $\Delta_{ii'} = E_i^g - E_{i'}^g = G$ [see Fig. 3(b)]. In the above sum we must include all transitions consistent with the magnetic dipole selection rules.

We assume that the source radiation has a Lorentzian line shape, and neglect any anisotropic f dependence. Substituting Eq. (6) into Eq. (5) and integrating over E gives

$$\frac{dI_M}{dx}(E',S) = \sum_{i,j,i'} \frac{I_0 nf^2\sigma_0(\frac{1}{2}\Gamma)^2(\frac{1}{2}\Gamma_b)^2 e^{-\mu_T(E'-\Delta_{ii'})\csc\alpha_1 x} W_{ij}W_{ji'}}{(1+\alpha')[(E'-\Delta_{ii'}-S)^2+(\frac{1}{2}\Gamma_b)^2][(E'-E_{ij}-\Delta_{ii'})^2+(\frac{1}{2}\Gamma)^2]} \,, \tag{7}$$

where Γ_b is the effective linewidth of the incident beam. Neglecting multiple scattering, the energy distribution of the nuclear resonant scattered radiation that gets to the detector is

$$I_M(E',S)=\int_0^T \frac{dI_M}{dx}(E',S)e^{-\mu_T(E')\csc\alpha_2 x}dx\ ,$$

where T is the thickness of the scatterer. The result is

$$I_M(E',S)=\sum_{i,j,i'}\frac{nf^2\sigma_0 I_0(\frac{1}{2}\Gamma)^2(\frac{1}{2}\Gamma_b)^2 W_{ij}W_{ji'}F_{MM}}{(1+\alpha')[(E'-\Delta_{ii'}-S)^2+(\frac{1}{2}\Gamma_b)^2][(E'-E_{ij}-\Delta_{ii'})^2+(\frac{1}{2}\Gamma)^2]}\ , \tag{8}$$

where

$$F_{MM}=\frac{1-\exp\{-T[\mu_T(E'-\Delta_{ii'})\csc\alpha_1+\mu_T(E')\csc\alpha_2]\}}{\mu_T(E'-\Delta_{ii'})\csc\alpha_1+\mu_T(E')\csc\alpha_2}\ .$$

Since in this experiment the energy of the scattered radiation is not determined, $I_M(E',S)$ has to be integrated over the energy parameter E' to obtain the measured intensity. Thus, the number of recoillessly absorbed and recoillessly emitted events is

$$N_{MM}(S)=\int_0^\infty I_M(E',S)dE'\ . \tag{9}$$

The number of recoillessly absorbed but nonrecoillessly emitted events N_{MN} can be obtained in the following way. First we must replace f^2 by $f(1-f)$ in Eq. (8). Then we must realize that, due to the recoil, the energy distribution of the emitted photon is "smeared out" over an energy region large compared to the hyperfine splitting. This requires that the factor F_{MM} in Eq. (8) be modified since the outgoing photon is not subject to resonant absorption in this case. In this way,

$$N_{MN}(S)=\int_0^\infty dE'\sum_{i,j,i'}\frac{nf(1-f)\sigma_0 I_0(\frac{1}{2}\Gamma)^2(\frac{1}{2}\Gamma_b)^2 W_{ij}W_{ji'}F_{MN}}{(1+\alpha')[(E'-\Delta_{ii'}-S)^2+(\frac{1}{2}\Gamma_b)^2][(E'-E_{ij}-\Delta_{ii'})^2+(\frac{1}{2}\Gamma)^2]}\ , \tag{10}$$

where

$$F_{MN}=\frac{1-\exp\{-T[\mu_T(E'-\Delta_{ii'})\csc\alpha_1+(\mu_e+\mu_R)\csc\alpha_2]\}}{\mu_T(E'-\Delta_{ii'})\csc\alpha_1+(\mu_e+\mu_R)\csc\alpha_2}\ .$$

Equations (8) and (10) are essentially the same as found in Debrunner and Morrison[28] but generalized to a "split" scatterer. The angular distribution of the resonantly scattered radiation is represented by $W_{ij}(\theta_1,\phi_1)W_{ji'}(\theta_2,\phi_2)$. If the scatterer is a powder, this factor must be averaged subject to the constraint that the scattering angle α is constant. We can denote this result by $W_{ij,ji'}(\alpha)$.

For calculational purposes it is convenient to use a notation where the transitions are labeled by the lines themselves as shown in Fig. 3(b). Then Eq. (8) can be written out explicitly,

$$\begin{aligned}I_M(E',S)=nf^2a_M\Bigg(&\sum_{i=1}^{6}\frac{W_{i,i}(\alpha)}{(E'-E_i)^2+(\frac{1}{2}\Gamma)^2}\,\frac{1-e^{-T(\csc\alpha_1+\csc\alpha_2)\mu_T(E')}}{[(E'-S)^2+(\frac{1}{2}\Gamma_b)^2](\csc\alpha_1+\csc\alpha_2)\mu_T(E')}\\&+\sum_{i=2}^{3}\frac{W_{i,i+2}(\alpha)(1-e^{-T[\mu_T(E'-G)\csc\alpha_1+\mu_T(E')\csc\alpha_2]})}{[(E'-E_i-G)^2+(\frac{1}{2}\Gamma)^2][(E'-S-G)^2+(\frac{1}{2}\Gamma_b)^2][\mu_T(E'-G)\csc\alpha_1+\mu_T(E')\csc\alpha_2]}\\&+\sum_{i=2}^{3}\frac{W_{i+2,i}(\alpha)(1-e^{-T[\mu_T(E'+G)\csc\alpha_1+\mu_T(E')\csc\alpha_2]})}{[(E'-E_{i+2}+G)^2+(\frac{1}{2}\Gamma)^2][(E'-S+G)^2+(\frac{1}{2}\Gamma_b)^2][\mu_T(E'+G)\csc\alpha_1+\mu_T(E')\csc\alpha_2]}\Bigg)\ ,\end{aligned} \tag{11}$$

where G equals the ground state splitting,

$$\mu_T(E')=\sum_{i=1}^{6}\frac{nf\sigma_0(\frac{1}{2}\Gamma)^2\bar{W}_i}{(E'-E_i)^2+(\frac{1}{2}\Gamma)^2}+\mu_R+\mu_e\ ,$$

and the bar indicates an average over all angles. Equation (10) can be similarly rewritten in this notation in a direct way.

In the above equations the W_i's are the dipole-radiation angular-distribution functions. The $W_{i,j}$'s are products of these functions and give the angular distribution for absorption at angle (θ_1,ϕ_1) and emission at (θ_2,ϕ_2). For the purpose of describing a powder scatterer the $W_{i,j}$'s have to be integrated over all angles consistent with the constraint that α, the scattering angle, remains constant. This integration has been presented elsewhere.[23] The results are

$$W_{1,1}=W_{6,6}=(3/8\pi)^2\tfrac{1}{4}(26+2\cos^2\alpha)/15,$$

$$W_{2,2}=W_{5,5}=(3/8\pi)^2\tfrac{4}{9}(6+2\cos^2\alpha)/15,$$

$$W_{3,3}=W_{4,4}=\tfrac{1}{9}W_{1,1}\ ,$$

$$W_{2,4}=W_{4,2}=W_{3,5}=W_{5,3}=(3/8\pi)^2\tfrac{1}{9}(14-2\cos^2\alpha)/15$$

The coherent nonresonant contribution to the scattered intensity is mostly Rayleigh, because at

these energies the Rayleigh contribution is ~ 10^4 times the Thomson contribution.[29] The energy dependence of the Rayleigh cross section is relatively weak and so

$$I_R(E'S) = \frac{I_0(\frac{1}{2}\Gamma_b)^2 n' f_R \sigma_R W_R(\alpha)}{(E'-S)^2 + (\frac{1}{2}\Gamma_b)^2} \times \frac{1 - e^{-\mu_T(E')(\csc\alpha_1 + \csc\alpha_2)T}}{\mu_T(E')(\csc\alpha_1 + \csc\alpha_2)} , \quad (12)$$

where n' is the number of atoms/volume, f_R is the recoilless fraction for Rayleigh scattering ($f_R = f^2$ for $\alpha = 90°$)[4], σ_R is the Rayleigh cross section evaluated at 14 keV (for our purposes), and[29]

$$W_R(\alpha) = \frac{1 + \cos^2\alpha}{\sin^3 \frac{1}{2}\alpha} = 2\sqrt{2} .$$

Collecting energy-independent factors and integrating over E',

$$N_R(S) = \int_0^\infty \frac{n' f_R a_R (1 - e^{-\mu_T(E')(\csc\alpha_1 + \csc\alpha_2)T}) dE'}{[(E'-S)^2 + (\frac{1}{2}\Gamma_b)^2]\,\mu_T(E')(\csc\alpha_1 + \csc\alpha_2)} . \quad (13)$$

The nonrecoilless Rayleigh contribution is

$$N_{NR} = \int_0^\infty \frac{dE' n' (1 - f_R) a_R (1 - e^{-[\mu_T(E')\csc\alpha_1 + (\mu_R + \mu_e)\csc\alpha_2]T})}{[(E'-S)^2 + (\frac{1}{2}\Gamma_b)^2][\mu_T(E')\csc\alpha_1 + (\mu_R + \mu_e)\csc\alpha_2]} . \quad (14)$$

The total intensity distribution of the scattered radiation is the sum of four terms given by Eqs. (9), (10), (13), and (14),

$$N(S) = N_{MM}(S) + N_{MN}(S) + N_R(S) + N_{NR}(S) . \quad (15)$$

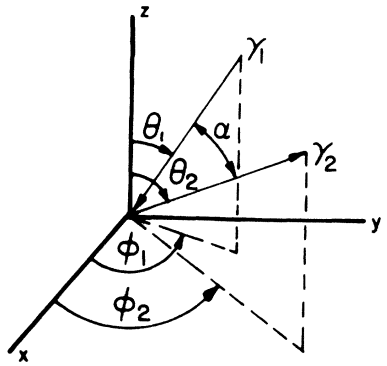

(a)

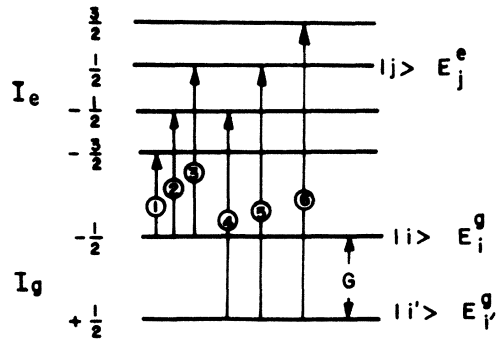

(b)

FIG. 3. (a) Various angles for the scattering process are defined as shown. (b) Nuclear energy levels and allowed transitions for $M1$ radiation in the case of ^{57}Fe.

The integrations over the energy parameter E' required to obtain the scattering spectrum given by Eq. (15) were accomplished by using standard numerical techniques.

In order to get some feeling for the various contributions in Eq. (15) we considered the case of an enriched iron-powder scatterer, and took the incident-beam linewidth to be negligible. From previous results,[23] the ratio of the nuclear resonant to Rayleigh contribution was known for our experiments. Figure 4 shows these calculated results taking the recoilless fraction and the linear absorption coefficient to be 0.7 and 205 cm^{-1}, respectively. In addition, β was set equal to 153 ($\beta = n\sigma_0 f$, see below). The top curve in Fig. 4 gives the nuclear recoilless-recoilless contribution. Notice that the second and fifth lines are taller than the first and sixth. This is a characteristic feature for thick scatterers. On the other hand, the second curve (from the top in Fig. 4) which gives the nuclear recoilless-nonrecoilless contribution shows all peaks to be the same height. This is familiar from Mössbauer *transmission* experiments using thick samples. The third curve, labeled R (in Fig. 4) shows the Rayleigh contribution, which for our case is rather small. Notice that there are dips at the Mössbauer resonance energies. This occurs because the Rayleigh cross section is essentially constant over this energy range, but the photons are absorbed preferentially at the resonance energies on passing into the thick scatterer. The bottom curve in Fig. 4 gives the final, combined result.

The rather unusual saturation effect (i.e., the ratio of peak heights as the thickness of the scatterer increases) in scattering experiments is ex-

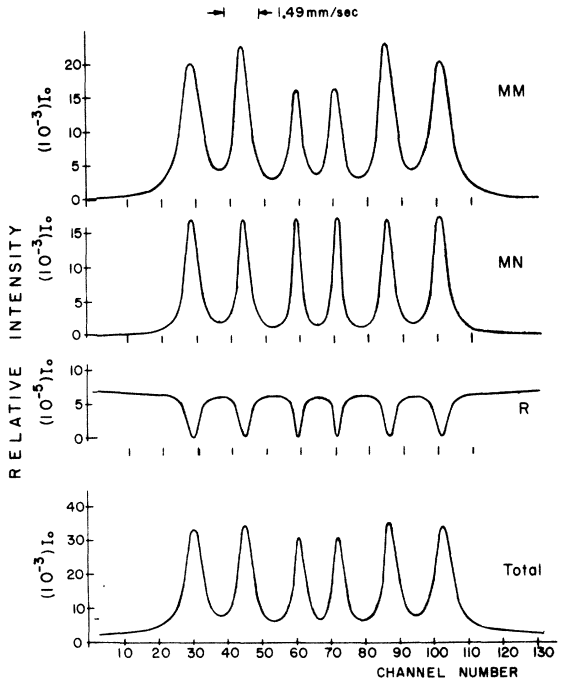

FIG. 4. Calculations showing the various contributions to the scattered Mössbauer spectrum. In these calculations the linewidth of the incident beam has been neglected. The scatterer is assumed to be a 91%-enriched iron powder having recoilless fraction of 0.7, linear-absorption coefficient 205 cm^{-1}, and thickness parameter $\beta(\beta = n\sigma_0 f)$ of 153. The top curve gives the nuclear recoilless-recoilless contribution. The next curve gives the nuclear recoilless-nonrecoilless part. The third curve from the top gives the Rayleigh contribution and the bottom curve gives the total result.

hibited more graphically in Fig. 5. In Fig. 5, we have plotted the relative nuclear resonant recoilless-recoilless intensities of the first three lines for an enriched iron-powder scatterer as a function of the thickness parameter β. Notice that above a certain value of β the second line becomes more intense and for large values of β the three intensities approach different limits.

The reason for this particular saturation effect can be understood in the following way. The nuclear resonant scattering process involves an absorption and a subsequent emission. Note, that when line 2 (or 3) is excited, the re-emission will occur at line 2 (3) and also at line 4 (5). Now the photons emitted at line 4 will be attenuated less than those at line 2 on passing through the scatterer on the way to the detector. Therefore, more photons will get to the detector than would if all the radiation were re-emitted at the energy of line 2. The opposite is true when line 3 is excited.

The total intensity distribution of the scattered radiation is given by Eq. (15). The results depend

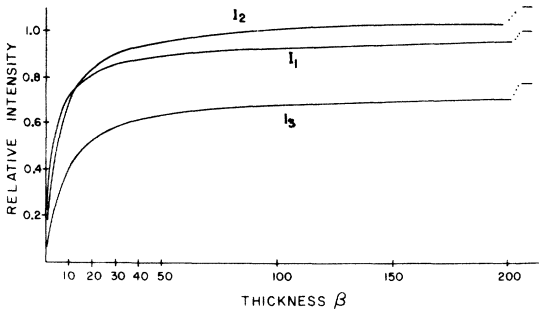

FIG. 5. Calculated saturation effect is shown for iron-powder scattering results. Notice the difference between such an effect in scattering as compared to ordinary transmission results. The curves are normalized so that $I_1 = 1$ at $\beta = \infty$.

on the value of the recoilless fraction (f) and the electronic absorption coefficient (μ_e). In Fig. 6, we show calculated spectra for an enriched iron-powder scatterer but using two different values of μ_e, namely, 200 and 800 cm^{-1}. We see that as μ_e increases we obtain an effectively thinner scatterer and hence, narrower lines. The peak intensities are also modified slightly.

In Fig. 7 we show the variation in the scattering line shape for different values of the recoilless fraction ($f = 0.2$, 0.7, and 1.0). The rather dramatic changes in the spectra indicate that such scattering experiments may be useful for measuring recoilless fractions.

III. EXPERIMENTAL RESULTS

The experiments were performed using a 15-mCi ^{57}Co in Cu source which was driven by a con-

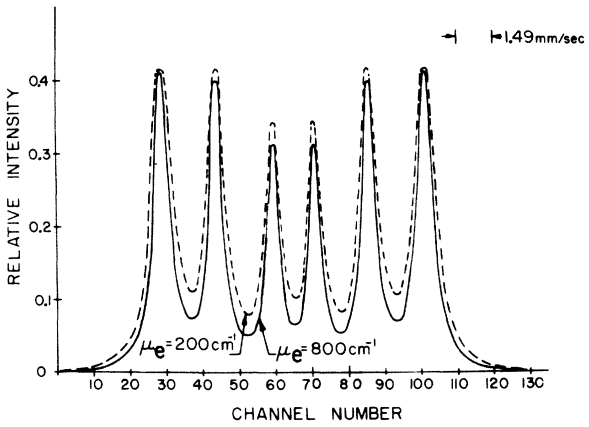

FIG. 6. Calculated results showing the effect of changing the electronic absorption coefficient μ_e on the Mössbauer scattering spectrum. We have assumed an enriched iron-powder scatterer with $f = 0.7$ and $\beta = 175$. The spectra are normalized to the same intensity for line 6.

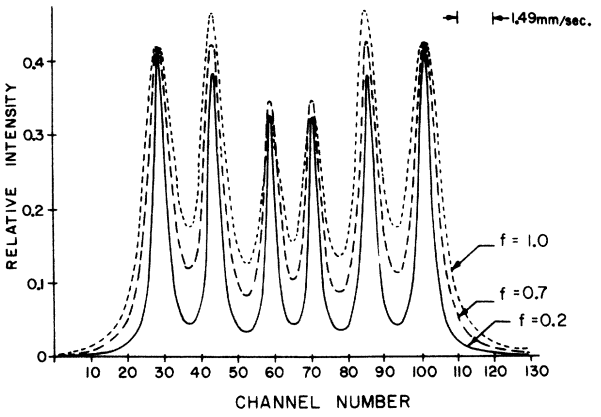

FIG. 7. Same as Fig. 6 but now the electronic absorption coefficient μ_e is fixed at 200 cm^{-1} and the recoilless fraction (f) takes on the values 0.2, 0.7, and 1.0.

ventional electromechanical drive. The scattering geometry is shown in Fig. 1. The angle defined by the incoming and outgoing photons is α, while χ_1 and χ_2 define the collimation of the incoming and outgoing beams. The source radiation was Doppler shifted by using a constant acceleration drive (CAD) and the scattered radiation detection by a proportional counter (Reuter-Stokes $XeCO_2$ at 2-atm pressure).

To protect the detectors from direct radiation we used a minimum of $\frac{1}{2}$-in. lead shielding. Both the source and detector were placed inside specially designed lead containers. All the lead surfaces facing the path of the incoming and outgoing beams were covered with $\frac{1}{16}$ in. of copper or brass plate to absorb the lead x rays. The mounting of the scatterer was made by pressing the sample powder, α-Fe_2O_3 or Fe metal, on a 0.010-in.-thick lucite

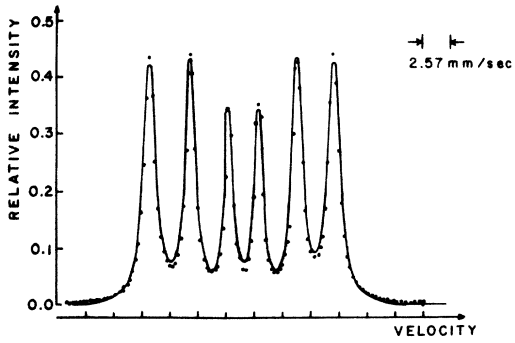

FIG. 8. Experimental and theoretical results for a 90% enriched α-Fe_2O_3 scatterer at room temperature. The dots give the experimental result. The solid curve is the theoretical result using $f = 0.8$, and $\beta = 322$. The theoretical result was obtained using only one free parameter; the percentage effect at one peak.

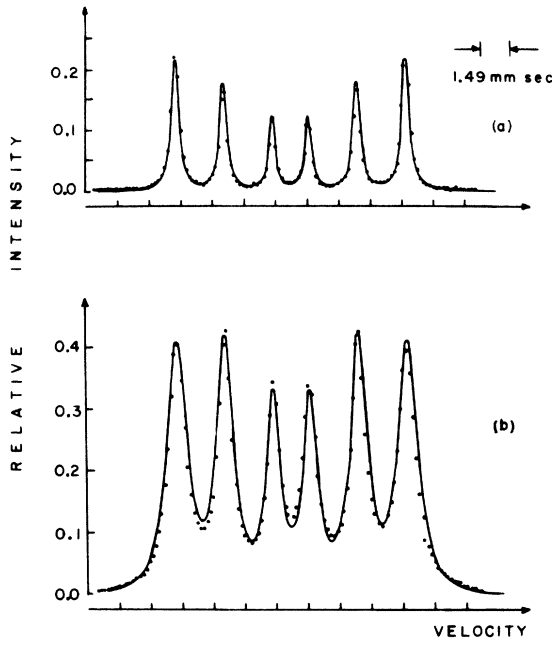

FIG. 9. (a) Experimental and theoretical scattering results for a $\frac{1}{8}$-in.-thick iron bar at room temperature having the natural content of ^{57}Fe. The dots are the data and the solid curve is the calculated result. The only free parameter is the percent effect at one peak. (b) Same kind of results as shown above but the scatterer is a 90% enriched iron powder ($f = 0.8$ and $\beta = 175$) at room temperature.

or beryllium disk containing a thin layer of vacuum grease to facilitate adhesion. A thin sheet of plastic Saran Wrap covered the powder. This combination was pressed into an aluminum frame and held in place by a tight fitting annular plug. The scatterer was supported in the path of the beam by a thin aluminum rod attached to a reference stand which allowed the scatterer to be rotated in the

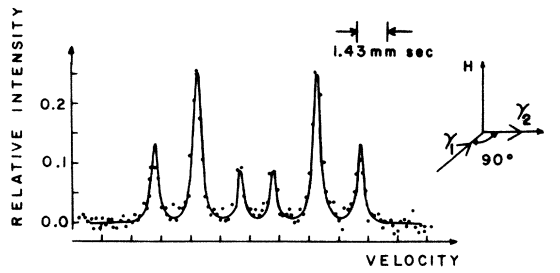

FIG. 10. Similar results to those shown in Fig. 9(a). However, in this case the iron bar has been placed in an external magnetic field of 5 kG. The orientation of the applied magnetic field is perpendicular to the plane defined by the incoming and scattered γ-ray beams. (The appropriate values of the $W_{i,j}$'s for this case were used in the calculation. Notice they are different from those used in the other calculations.)

horizontal plane. The scatterer was mounted in this way to reduce as much of the extraneous nonresonant scattered radiation as possible.

In analyzing scattering experiments it is important to know the energy distribution of the source radiation. This distribution, which includes thickness effects in the source, finite source area, collimation, and mechanical distortions, was measured by conducting constant-velocity transmission experiments using a thin absorber. The measured effective linewidth of our ^{57}Co in Cu source was $\Gamma_b = 2.3\Gamma$, where $\Gamma = 0.097$ mm/sec.

All our experiments were done using ^{57}Fe, and the calculations were performed assuming that the nuclear levels are pure m states. As noted above, $\alpha = 90°$ and $\alpha_1 = \alpha_2 = 45°$. The E_i's and G used in Eq. (11) in Sec. II can be determined by ordinary transmission experiments. The linear-absorption coefficient, $\mu = \mu_R + \mu_e$, was determined experimentally for both iron and α-Fe_2O_3 samples by measuring the attenuation of an off-resonance γ-ray beam on passing through various sample thicknesses. The values obtained were: $\mu = 205$ cm^{-1} for iron and $\mu = 54$ cm^{-1} for α-Fe_2O_3. The relative strength of Rayleigh to Mössbauer processes, i.e., (a_R/a_M) [see Eqs. (11) and (13)] can be calculated.[29] This result was checked by performing selective-excitation–double-Mössbauer (SEDM) experiments which are described elsewhere.[23,30] These SEDM experiments gave $a_R/a_M = 4\times10^{-5}$ for α-Fe_2O_3, and 3.8×10^{-5} for iron.

Three scatterers were used in this work, an enriched α-Fe_2O_3 scatterer, an enriched iron-powder scatterer, and an iron bar $\frac{1}{8}$ in. thick. The single-line-thickness parameters, β ($\beta = n\sigma_0 f$, where n = number of ^{57}Fe atoms/cm^2, σ_0 is resonance cross section, and f is the recoilless fraction), for the enriched samples were calculated from the known amount of ^{57}Fe in the samples. For the enriched α-Fe_2O_3 scatterer $\beta = 322$ and for the enriched iron-powder scatterer $\beta = 175$. Figure 8 shows a scattering spectrum obtained with an enriched powder sample of α-Fe_2O_3. The solid curve in the figure represents the spectrum calculated by using Eq. (15) and the appropriate input parameters. The only free parameter is the percentage effect of one of the lines. Note the characteristic thick-scatterer saturation effect which we have discussed above and which is quite different from the well-known transmission-geometry saturation effect.

In Fig. 9 we show experimental and calculated results for an iron bar and a 90% enriched iron powder.

In Fig. 10 we again show results for the iron bar $\frac{1}{8}$ in. thick having a natural content of ^{57}Fe. In this case, however, the bar was placed between the poles of a permanent 5-kG magnet. In this case the incident and scattered beams form an angle of 90° and lie in a plane perpendicular to the magnetic field, as shown in the diagram to the right of the spectrum. Again the solid curve gives the one-parameter calculated line shape obtained for the real scatterer, according to Eq. (15).

IV. CONCLUSIONS

We have developed calculational procedures for interpreting ^{57}Fe Mössbauer scattering experiments. Our calculations and experimental results show that incoherent thickness effects must be included in order to obtain satisfactory agreement. Of particular interest was the experimental and theoretical result that showed a saturation-line intensity effect that was quite different from the transmission result. This result is essentially due to incoherent thickness effects. Our calculations can be extended so that it would be possible to obtain hyperfine interaction parameters from scattering data, as has been done for transmission results for some time.

Debrunner and Morrison[28] have discussed the determination of the recoilless fraction from Mössbauer scattering experiments using a single-line scatterer. Our calculations show that the scattering line shape can be a rather strong function of the recoilless fraction when using a "split" scatterer. In fact, we believe it would be easier to unambiguously determine the recoilless fraction for a multilined scatterer.

---

*Work supported by the National Science Foundation (Grant No. GH-39137).

[1]S. Bernstein and E. C. Campbell, Phys. Rev. 132, 1625 (1963).
[2]V. K. Voitevetskii, I. L. Korsumskii, A. I. Novikov, and Yu. Pazhin, Zh. Eksp. Teor. Fiz. 54, 1361 (1968) [Sov. Phys.-JETP 27, 729 (1968)].
[3]P. J. Black, D. E. Evans, and D. A. O'Connor, Proc. R. Soc. A 270, 168 (1962).
[4]P. J. Black, G. Longworth, and D. A. O'Connor, Proc. Phys. Soc. Lond. 83, 925 (1964).
[5]P. J. Black, G. Longworth, and D. A. O'Connor, Proc. Phys. Soc. Lond. 83, 937 (1964).
[6]J. K. Major, Nucl. Phys. 33, 323 (1962).
[7]C. Tzara and R. Barloutand, Phys. Rev. Lett. 4, 405 (1960).
[8]D. A. O'Connor and N. M. Butt, Phys. Lett. 7, 233 (1963).
[9]P. J. Black and I. P. Duerdoth, Proc. Phys. Soc. Lond. 84, 169 (1964).
[10]J. Olsen, Nucl. Instrum. Meth. 70, 109 (1969).
[11]P. Thieberger, J. A. Moragues, and A. W. Sunyar, Phys. Rev. 171, 425 (1968).
[12]M. Atac, P. Debrunner, and H. Frauenfelder, Phys. Lett. 21, 699 (1966).
[13]R. L. Collins, *Mössbauer Effect Methodology*, edited

by L. J. Gruverman (Plenum, New York, 1968), Vol. 4, p. 129.
[14]Z. W. Bonchev, A. Jordanov, and A. Minkova, Nucl. Instrum. Meth. 70, 36 (1969).
[15]K. R. Swanson and J. J. Spijkerman, J. Appl. Phys. 41, 3155 (1970).
[16]H. J. Lipkin, Phys. Rev. 123, 62 (1961).
[17]D. A. O'Connor and P. J. Black, Proc. Phys. Soc. Lond. 83, 941 (1964).
[18]I. P. Dzub, and A. F. Lubchenko, Fiz. Tverd. Tela 3, 275 (1961) [Sov. Phys.-Solid State 3, 1651 (1962)].
[19]V. A. Belyaev and Yu. M. Aivazyan, Zh. Eksp. Teor. Fiz. Pis'ma Red. 7, 477 (1968) [Sov. Phys.-JETP Lett. 7, 368 (1968)].
[20]Yu. M. Aivazyan and V. A. Belyakov, Zh. Eksp. Teor. Fiz. 56, 346 (1969) [Sov. Phys.-JETP 29, 191 (1969)].
[21]Yu. Kagan, A. M. Afanasev, and I. P. Perstnev, Zh. Eksp. Teor. Fiz. 54, 1530 (1968) [Sov. Phys.-JETP 27, 819 (1968)].
[22]Yu. Kagan, and A. M. Afanasev, Zh. Eksp. Teor. Fiz. 50, 271 (1966) [Sov. Phys.-JETP 23, 178 (1966)].
[23]B. Balko and G. R. Hoy, *Mössbauer Effect Methodology*, Vol. 9, edited by I. J. Gruverman (Plenum, New York, 1974); Phys. Lett. A 47, 171 (1974); Phys. Rev. B 10, 36 (1974).
[24]See, for example, G. R. Hoy and S. Chandra, J. Chem. Phys. 47, 961 (1967).
[25]B. Balko, Ph. D. dissertation (Boston University, 1973) (unpublished).
[26]A. M. Arem'ev, V. V. Sklyarevskii, G. V. Smirnov, and E. P. Stepanov, (report of research prior to publication, 1973).
[27]A. J. F. Boyle and H. E. Hall, Prog. Phys. 25, 441 (1962).
[28]P. Debrunner and R. J. Morrison, Rev. Sci. Instrum. 36, 145 (1965).
[29]P. B. Moon, Proc. Phys. Soc. A 63, 80 (1950).
[30]B. Balko and G. R. Hoy, Bull. Am. Phys. Soc. 19, 479 (1974).